

1 **Revised version 3**

2 **Ca $L_{2,3}$ -edge near edge X-ray absorption fine structure of tricalcium aluminate,**
3 **gypsum and calcium (sulfo)aluminate hydrates**

4

5 Guoqing Geng ^{1,*}, Rupert J. Myers ^{1,4}, Arthur L. D. Kilcoyne ², Juyoung Ha ³, Paulo J. M.
6 Monteiro ^{1,2}

7

8 ¹ Department of Civil and Environmental Engineering, University of California, Berkeley,
9 California 94720, United States

10

11 ² Advanced Light Source, Lawrence Berkeley National Laboratory, Berkeley, California
12 94720, United States

13

14 ³ School of Environmental and Sustainability Sciences, Kean University, Union, New
15 Jersey 07083, United States

16

17 ⁴ School of Forestry & Environmental Studies, Yale University, 195 Prospect Street, New
18 Haven, Connecticut 06511, United States

19

20

21 *Corresponding author: tel.: +1 510 590 2744; e-mail: guoqinggeng1989@gmail.com.

22

23

24
25
26
27
28
29
30
31
32
33
34
35
36
37
38
39
40
41
42
43
44
45
46

Abstract

Tricalcium aluminate (cement clinker phase), gypsum, katoite, ettringite and calcium monosulfoaluminate hydrate (abbreviated as kuzelite) are the major minerals in the hydration reaction of tricalcium aluminate in the presence of gypsum and have critical impacts on the kinetics and thermodynamics of early-age cement hydration mechanisms. Here, spectroscopic analysis of these minerals is conducted using scanning transmission X-ray microscopy (STXM). Their Ca $L_{2,3}$ -edge near edge X-ray absorption fine structure (NEXAFS) spectra are measured and correlated to the known Ca coordination environments. The results indicate that these minerals have unique Ca environments that can be differentiated from one another based on the intensities and positions of the absorption peaks at 346.5-348.5 eV and 350.5-351.5 eV. It is concluded that Ca in tricalcium aluminate (cubic and orthorhombic polymorphs) and katoite is in cubic-like coordination with negative $10Dq$, whereas Ca is in an octahedral-like coordination with positive $10Dq$ in ettringite, gypsum and kuzelite. For tricalcium aluminate, the Ca atoms in both polymorphs are in similar chemical environments with slightly more distortion in the orthorhombic polymorph. As a common issue in STXM experiments, absorption saturation of NEXAFS spectra is also investigated. It is demonstrated that the optical density difference between pre- and post-edge absorption levels provides a reliable indication of the sample thickness in the systems studied. The present work provides a reference for STXM study of the calcium (sulfo)aluminate reaction system in cement hydration and natural aqueous environments.

47 **Keywords:** Tricalcium aluminate, calcium aluminate hydrate, calcium sulfoaluminate
48 hydrate, STXM, NEXAFS, Ca $L_{2,3}$ -edge, absorption saturation

49

50

Introduction

51 Calcium (sulfo)aluminate hydrates are found in geological formations (Bell and
52 Rossman 1992; Nelson 1982), wet near-surface environments (Puppala et al. 2005; van
53 Aardt and Visser 1977), and complex composite materials such as hydrated Portland
54 cement (PC) (Taylor 1997; Mehta and Monteiro 2006). Recent studies suggest that heavy
55 metal oxyanions, such as chromate (Hashem and Amin 2014), arsenate (Sasaki et al.
56 2014) and selenate (Baur and Johnson 2003), can be immobilized using calcium
57 (sulfo)aluminate hydrates, e.g., ettringite (Chrysochoou and Dermatas 2006; Zhou et al.
58 2006; Hillier et al. 2007), as these elements can be directly substituted into the structures
59 of these minerals. The substitution extent of heavy metal oxyanions has been shown to
60 depend on the coordination environment of Ca with respect to sulfate. It has also been
61 suggested that the coordination environment of Ca is a critical parameter in determining
62 the reactivity of minerals (Davidovits 1994; Skibsted et al. 1993; Black et al. 2003). The
63 Ca coordination symmetry of many natural and synthetic solid phases has been studied
64 by Ca $L_{2,3}$ -edge NEXAFS (Solomon et al. 2012; Ha et al. 2012; Jackson et al. 2013; Geng
65 et al. 2015; Fleet and Liu 2009). The peak structures and separations at the absorption
66 edges are affected by the crystal field splitting and spin-orbit effects (Stöhr 2013).
67 Nanometer-resolved identification of Ca coordination environments in complex
68 composite materials (e.g., hydrated cement) has been reported but seems challenging due
69 to the lack of direct links between NEXAFS spectra and coordination configurations

70 (Solomon et al. 2012; Jackson et al. 2013). The efficient assignment of spectra to mineral
71 phases greatly relies on understanding the reference spectra of known minerals and semi-
72 empirical prediction of coordination environment from the spectra details.

73

74 Scanning transmission X-ray microscopy (STXM) combines spatially resolved
75 measurements with X-rays of tunable energy at synchrotron radiation facilities (Warwick
76 et al. 2002; Kilcoyne et al. 2003). The bonding and coordination environments of Ca in
77 calcium (sulfo)aluminate hydrates intermixed on the nano- and microscales can be
78 spatially determined by STXM using coupled near edge X-ray absorption fine structure
79 (NEXAFS) measurements (Stöhr 2013). This technique has gained significant interest in
80 geology (Wan et al. 2007), environmental and material research applications (Chen et al.
81 2014), photovoltaics (McNeill et al. 2008) and cosmological chemistry (Sandford et al.
82 2006). Cement hydration systems have submicron chemical and structural heterogeneities
83 that greatly influence their macroscopic performances, e.g., rheology, hydration heat
84 release and volumetric stability. STXM provides a powerful analytical tool for measuring
85 both spectroscopic and spatial information down to the micro- or nanometer scales for
86 cementitious materials; however, collecting reference spectra of cement-based minerals is
87 critical for analyzing the spatially resolved spectroscopic data.

88

89 Tricalcium aluminate ($3\text{CaO}\cdot\text{Al}_2\text{O}_3$, abbreviated as C_3A) is a clinker mineral whose
90 hydration determines the early-age performance of fresh concrete mixtures. It is cubic
91 ($\text{C}_3\text{A}_{\text{cub}}$) when the Na_2O mass content is less than 1.9 wt% and orthorhombic ($\text{C}_3\text{A}_{\text{orth}}$)
92 when the Na_2O doping is between 3.5 wt% and 4.2 wt% (Barnes and Bensted 2002). Its

93 direct reaction with water rapidly forms metastable calcium aluminate hydrates, which
94 quickly become katoite ($3\text{CaO}\cdot\text{Al}_2\text{O}_3\cdot 6\text{H}_2\text{O}$, a garnet structure type mineral). In the
95 presence of gypsum ($\text{CaSO}_4\cdot 2\text{H}_2\text{O}$), the hydration speed is adjusted by the slow
96 formation of ettringite ($3\text{CaO}\cdot\text{Al}_2\text{O}_3\cdot 3\text{CaSO}_4\cdot 32\text{H}_2\text{O}$), which is later transformed into
97 calcium monosulfoaluminate hydrate, i.e. kuzelite ($3\text{CaO}\cdot\text{Al}_2\text{O}_3\cdot\text{CaSO}_4\cdot 12\text{H}_2\text{O}$) through
98 reaction with remnant C_3A after the gypsum is completely consumed (Barnes and
99 Bensted 2002). In this project, STXM is used to collect the reference Ca $L_{2,3}$ -edge
100 NEXAFS spectra of several calcium (sulfo)aluminate hydrate mineral phases. The
101 correlations between the spectral features and Ca coordination environments are
102 discussed. The influence of the absorption saturation on the correct interpretation of the
103 Ca $L_{2,3}$ -edge NEXAFS spectra is also studied. This work provides reference spectra for
104 the STXM study of calcium (sulfo)aluminate reaction systems in cement hydration and
105 natural aqueous environments.

106

107

Ca $L_{2,3}$ -edge NEXAFS theory

108 The crystal field splitting of d^0 compounds such as Ca^{2+} has been investigated
109 experimentally and theoretically (Figure 1) to understand the link between coordination
110 symmetry and near-edge adsorption fine structure (de Groot et al. 1990; Burns 1993;
111 Albright et al. 2013). The lowest unoccupied molecular orbitals (LUMOs) in the CaO_x
112 complex are t_{2g} and e_g . They are close in energy but distinct in symmetry. The t_{2g} state is
113 mainly composed of d_{xy} , d_{yz} and d_{xz} orbitals and therefore has the same symmetry as these
114 orbitals, whereas e_g is mainly composed of d_z^2 and $d_{x^2-y^2}$ orbitals. In the isolated Ca^{2+} ion,
115 the t_{2g} and e_g states share the same energy, but when approached by coordinating oxygens,

116 their energies become significantly different. The t_{2g} state is at a higher energy than the e_g
117 state when Ca coordination is in cubic symmetry whereas the opposite is true for
118 octahedral symmetry. Therefore, the energy gap (e_g-t_{2g}), equivalently termed $10Dq$, is
119 negative for cubic symmetry and positive for octahedral symmetry. A typical Ca $L_{2,3}$ -
120 edge NEXAFS spectra has two major peaks (a_2 and b_2), two minor peaks (a_1 and b_1), and
121 several leading peaks (1, 2 possibly). The spin-orbital interaction splits the Ca $L_{2,3}$ -edge
122 NEXAFS spectra into two doublets. The lower-energy doublet (a_1 and a_2) corresponds to
123 excitation from $2p_{3/2}$ orbitals whereas the higher-energy doublet (b_1 and b_2) corresponds
124 to excitation from $2p_{1/2}$ orbitals. In each doublet, the major peak corresponds to a final
125 state of the higher energy state in t_{2g} and e_g , while the lower one corresponds to the minor
126 peak. The peak position differences a_2-a_1 and b_2-b_1 are determined by, but not identical to,
127 $10Dq$ (de Groot et al. 1990). The leading peaks 1, 2 and b_{1o} are part of the multiplet
128 spectrum and can be accounted for by the Coulomb repulsion and exchange terms (de
129 Groot et al. 1990). In cubic coordination, the minor peak 2 occurs between the energies of
130 the a_1 and a_2 peaks, which can be used to distinguish between cubic and octahedral
131 coordination symmetries.

132

133 In a Ca $L_{2,3}$ NEXAFS spectrum, peak broadening is caused by the solid-state broadening
134 effect when the sample becomes thicker and disorder appears in the crystal structures,
135 which increases the number of inter-peak absorption states (Obst et al. 2009). The
136 intensities of the minor peaks also increase more rapidly than those of the major peaks
137 with increasing sample thickness. A previous study concluded that peak heights should
138 not exceed 0.30 ± 0.05 OD (optical density) to obtain reliable spectra with no absorption

139 saturation artifacts, corresponding to a sample thickness of 30 nm (Hanhan et al. 2009).
140 However, conditions vary from beamline to beamline. Quantitative NEXAFS spectra
141 with no saturation artifacts can be obtained using beamline 5.3.2.2 at the ALS of the
142 Lawrence Berkeley National Laboratory for OD values of ~ 1.0 , corresponding to a
143 sample thickness of ~ 200 nm. Saturation effects are generally significant in the analysis
144 of NEXAFS spectra of cement systems, as the typical grain size distribution in cement
145 varies from ~ 100 nm to ~ 100 μm .

146

147

Materials and Methods

148 To ensure purity, all samples studied here were lab-prepared phases, rather than from
149 natural sources. Katoite, ettringite, $\text{C}_3\text{A}_{\text{cub}}$ and $\text{C}_3\text{A}_{\text{orth}}$ powders were purchased from
150 Mineral Research Processing (<http://www.mineralresearchprocessing.fr/>). The crystal
151 structures and chemical compositions of these minerals were verified by powder X-ray
152 diffraction (XRD) (Electronic Supporting Information). Gypsum was purchased from
153 Fisher Scientific (#S76764). Ca $L_{2,3}$ -edge NEXAFS spectra of katoite, ettringite, $\text{C}_3\text{A}_{\text{cub}}$
154 and $\text{C}_3\text{A}_{\text{orth}}$ were measured on samples prepared by drop-casting small amounts of these
155 precursors directly onto Si_3N_4 windows. Ca $L_{2,3}$ -edge NEXAFS spectra of kuzelite was
156 obtained by spectromicroscopic analysis of samples produced by mixing gypsum, $\text{C}_3\text{A}_{\text{cub}}$
157 and deionized water by hand at a mass ratio of 0.4:1:14 in sealed plastic vials under
158 ambient conditions (1 atm, 25 ± 2 °C). Small volumes (~ 0.2 μL) of the hydrated mixtures
159 were drop-cast onto 100-nm-thick Si_3N_4 windows (Norcada) after 9 days of reaction. The
160 reactions were stopped by removing excess water immediately after drop-casting by
161 gently contacting the mixtures with Kimwipes (Kimtech Science), leaving a thin layer of

162 hydrated solids (Figure 2) (Kilcoyne et al. 2003). Ca $L_{2,3}$ -edge NEXAFS spectra of
163 katoite and C_3A_{cub} were measured on samples prepared by drop-casting small amounts of
164 these precursors directly onto Si_3N_4 windows.

165

166 The STXM and Ca $L_{2,3}$ -edge NEXAFS measurements were conducted at beamline
167 5.3.2.2 of the Advanced Light Source (Lawrence Berkeley National Laboratory), which
168 operates at 1.9 GeV and 500 mA using a bending magnet source and an active servo-
169 stabilized toroidal pre-mirror. Two computer-controlled slits are placed on each side of a
170 low dispersion spherical grating monochromator. Within the energy range of 250-780 eV,
171 the resolving power of the radiation source at beamline 5.3.2.2 is $E/\Delta E \sim 5000$ when
172 using slit dimensions of approximately $20 \times 10 \times 10 \mu\text{m}$ and decreases to $E/\Delta E \sim 2000$
173 with slit dimensions of approximately $60 \times 30 \times 30 \mu\text{m}$, where E is the incident beam
174 energy and ΔE is the resolvable energy step size. The scanning transmission X-ray
175 microscope installed on beamline 5.3.2.2 has a spatial scanning resolution limit of ~ 31
176 nm utilizing a $240 \mu\text{m}$ diameter zone plate, with the transmission signal recorded using a
177 phosphor-coated photomultiplier tube (PMT) (Stöhr 2013; Collins and Ade 2012). The
178 photon energy is calibrated by setting the position of the Rydberg $3s$ peak for CO_2 to
179 292.74 eV as detailed in reference (Collins and Ade 2012).

180

181 Samples were measured under 0.3 atm of helium. The energy scanning range was set to
182 340-360 eV, with a step size of 0.1 eV between 345 and 356 eV and a step size of 0.2 eV
183 used at the other sampled energies. The measured data were processed using aXis2000
184 software (Hitchcock et al. 2012).

185

186

Results and Discussion

187 Ca $L_{2,3}$ -edge NEXAFS Spectra and Crystal Chemistry

188 The Ca $L_{2,3}$ -edge NEXAFS spectra of all the studied minerals show fine structures within
189 the energy range of 346 to 354 eV (Figure 3), consistent with Ca $L_{2,3}$ -edge NEXAFS
190 spectra of many Ca-containing minerals (Solomon et al. 2012; Ha et al. 2012; Jackson et
191 al. 2013; Geng et al. 2015; Fleet and Liu 2009). Unique spectra were repeatedly observed
192 for each mineral phase on different sampling regions of similar thickness, indicating that
193 the chemical environment of Ca in each mineral is relatively homogeneous at the spatial
194 resolution of ~ 30 nm.

195

196 **Katoite.** The shape of the Ca $L_{2,3}$ -edge NEXAFS spectrum of katoite (Figure 3) is similar
197 to that of CaF_2 (de Groot et al. 1990; Naftel et al. 2001; Miedema et al. 2011), which
198 contains Ca coordinated to eight F atoms in cubic symmetry. The cubic-like symmetry of
199 katoite is confirmed by the larger peak energy differences of a_2 - a_1 (1.70 eV) than b_2 - b_1
200 (1.21 eV) in this phase. A similar a_2 - a_1 energy difference is found for CaF_2 (1.60-1.70
201 eV), although the b_2 - b_1 energy difference in CaF_2 (1.40-1.44 eV) is larger. According to
202 Lager et al. (1987), all Ca and O atoms are in equivalent positions in katoite. Figure 4a
203 shows that each Ca atom is coordinated to eight O atoms, half with Ca-O bond lengths of
204 2.360 Å and half with Ca-O bond lengths of 2.514 Å. Along the two-fold rotation axis,
205 the top four O atoms are labelled O_t and the bottom four are labelled O_b . The
206 coordination symmetry of Ca in katoite is distorted from perfect cubic symmetry in two
207 ways: (1) the different Ca-O bond lengths modify the positions of O atoms in the top and

208 bottom planes of the structure to rectangular rather than square shapes; and (2) there is a
209 slight misalignment of the top and bottom rectangles (Figure 4a).

210

211 **Ettringite.** The Ca $L_{2,3}$ -edge NEXAFS spectrum of ettringite (Figure 3a) resembles that
212 of octahedrally coordinated Ca both because the peak energy differences of a₂-a₁ and b₂-
213 b₁ are comparable and because no peak is observed between a₁ and a₂. The leading peak
214 2 is almost indistinguishable in this spectrum. The energy differences between the peak
215 positions a₂ and a₁ at the L_3 edge and b₂ and b₁ at the L_2 edge are 1.05 eV and 1.14 eV,
216 respectively, which are low relative to the corresponding values for calcite and calcium
217 hydroxide (Geng et al. 2015). The relatively low splittings of the L_3 and L_2 edges and low
218 intensities of the minor a₁ and b₁ peaks indicate a weak crystal field.

219

220 So far three ettringite structures have been reported where Ca environments are highly
221 comparable (Moore and Taylor 1970; Hartman and Berliner 2006; Goetz and Neubauer
222 2006). Ettringite contains eight-fold coordinated Ca in two positions (Figure 4b), with
223 Ca-O bond lengths for Ca1 ranging from 2.356 Å to 2.739 Å, average of 2.464 Å, and
224 those for Ca2 ranging from 2.317 Å to 2.747 Å, average of 2.491 Å (Moore and Taylor
225 1970). Viewing Ca1 along the (100) axis, the corners of the rectangle formed by two O1
226 atoms and two O3 atoms are misaligned with the corners of the rectangle formed by O6,
227 O8, O10 and O12 atoms, and thus, the t_{2g} orbital is less destabilized by the ligands.
228 Instead, the O8 atom and two O1 atoms can destabilize the d_z^2 orbital from the axial
229 direction and the five equatorial oxygen atoms, i.e., O6, O10, O12 and two O3 atoms can
230 destabilize the $d_{x^2-y^2}$ and d_{xy} orbitals (note that O6 and O12 are slightly off the equatorial

231 plane to the O8 side). In contrast, the d_{yz} and d_{xz} orbitals are less likely to be destabilized
232 because their symmetry poorly matches that of the ligand configuration. Ca2 has a very
233 similar configuration to Ca1, with O7 and O2 in axial positions and O5, O9, O11, O4s in
234 equatorial positions. Based on the above reasoning, we predict that Ca in ettringite is in a
235 weak crystal field with positive $10Dq$. This matches very well with the Ca $L_{2,3}$ -edge
236 NEXAFS spectrum of ettringite in Figure 3a.

237

238 **Kuzelite.** The Ca $L_{2,3}$ -edge NEXAFS spectra for kuzelite and ettringite are similar,
239 except that the positions of the a_2 , b_1 and b_2 peaks in the former phase are shifted to lower
240 energy, which also has a relatively smaller L_3 splitting (0.93 eV) and a relatively larger L_2
241 splitting (1.18 eV). The Ca $L_{2,3}$ -edge NEXAFS spectrum for kuzelite contains very well
242 resolved leading (1, 2) and minor (a_1 , b_1) peaks and has a relatively high signal to noise
243 ratio, which can be attributed to the analysis of large, uniformly thick and near-perfect
244 hexagonal crystals (Figure 3c).

245

246 In kuzelite, there is one equivalent Ca position (Allmann 1977) (Figure 4c). The oxygen
247 in water (O_w) is located on the (001) axis (threefold rotation axis) 2.497 Å from the
248 central Ca atom; three hydroxyl O atoms in hydroxyl groups, labelled O_{hd} , are
249 equatorially coordinated with bond lengths of 2.375 Å; another three O_{hd} atoms are
250 coordinated to the central Ca atom from the opposite side of O_w with a bond length of
251 2.455 Å (referred as top O_{hd} atoms as viewed from the perspective shown in Figure 4c,
252 where the side that the rotation axis is pointing toward is denoted as the top side). There
253 is a misalignment of 43.7° in the orientations of the equatorial O_{hd} regular triangle (blue

254 triangle in Figure 4c inset) and the top O_{hd} regular triangle (red triangle in Figure 4c
255 inset). In this configuration, only the d_z^2 orbital is likely to be significantly destabilized,
256 axially by O_w , on top by the O_{hd} triangle, and equatorially by the equatorial O_{hd} triangle.
257 Compared with the strong destabilization of the perfect octahedral ligand configuration
258 (Moore and Taylor 1970), we expect the Ca $L_{2,3}$ -edge NEXAFS spectra for kuzelite to be
259 similar to those with small positive $10Dq$, which matches the result shown in Figure 3a.

260

261 **Gypsum.** The Ca $L_{2,3}$ -edge NEXAFS spectrum measured for gypsum is similar to the
262 spectra obtained for ettringite and kuzelite (Figure 3a), although the L_3 edge peak
263 splitting (a_2-a_1) of 0.85 eV and the L_2 edge peak splitting (b_2-b_1) of 0.90 eV for gypsum
264 are smaller, indicating a weaker crystal field. Values of L_3 and L_2 edge splitting of ~ 0.95
265 eV have previously been reported for $CaSO_4$, indicating a stronger crystal field with
266 emission of crystalliferous water (Patel and Aswath 2012). The Ca $L_{2,3}$ -edge NEXAFS
267 spectrum for gypsum also contains weak leading 1 and 2 peaks and shows a small,
268 positive $10Dq$ value because peak 2 is located between peak 1 and a_1 . There is an
269 additional weak b_{10} peak at 350.82 eV, which was not identified in the NEXAFS of
270 perfectly octahedral coordinated compounds nor in theoretical calculations (de Groot et al.
271 1990). Therefore, the NEXAFS results for gypsum indicate that this phase contains Ca in
272 distorted coordination symmetry with $3d$ orbitals destabilized in a way similar to
273 octahedral coordination.

274

275 The analysis for gypsum presented above is consistent with the crystal chemistry of Ca in
276 this phase (Comodi et al. 2008). In gypsum, Ca is coordinated to eight oxygen atoms in

277 one equivalent position (Figure 4d), with bond lengths ranging from 2.360 Å to 2.547 Å.
278 The relative orientation of the two O₂ atoms and two O_w atoms to the four O₁ atoms in
279 gypsum and katoite are similar if viewed along the (010) axis (i.e., the rotation axis),
280 although neither the O₂, O_w nor O₁ atoms lie in the same plane. From the geometric
281 point of view, the coordination of Ca in gypsum can be classified into neither octahedral-
282 like nor cubic-like symmetry but rather a spherical-like symmetry, with 8 ligand O atoms
283 distributing randomly within short range of distances from the center Ca. This leads to a
284 much weaker splittings at the L_3 and L_2 edges than in ettringite and kuzelite.

285

286 **Cubic and orthorhombic C₃A.** The Ca $L_{2,3}$ -edge NEXAFS spectrum C_3A_{cub} exhibits a
287 cubic-like symmetry pattern with peak 2 located between the positions of peaks a_1 and a_2
288 with L_3 and L_2 edge splittings of 1.57 eV and 1.28 eV, respectively.

289

290 There are six Ca sites in the C_3A_{cub} unit cell (Mondal and Jeffery 1975) (Figure 5). Ca1
291 and Ca2 have identical site symmetry and are in a distorted octahedral configuration with
292 Ca-O bond lengths of 2.338 Å. All three oxygen pairs in Ca1 and Ca2 take Ca as the
293 center, yet the angles between these pairs are 79.2° instead of 90°. Ca3 is also distorted
294 from octahedral coordination with three 2.352 Å-long Ca-O bonds and three 2.356 Å-
295 long Ca-O bonds. The angle of each O3-Ca-O4 bond is 162.52°. The four equatorial O
296 atoms are not exactly coplanar. The coordination structures of Ca4, Ca5 and Ca6 are
297 more complex, with Ca-O bond lengths varying between 2.258 Å and 3.013 Å. Therefore,
298 Ca $L_{2,3}$ -edge NEXAFS spectrum for C_3A_{cub} is a superposition of contributions from
299 octahedrally coordinated Ca (Ca1, Ca2 and Ca3) and irregularly coordinated Ca (Ca4,

300 Ca5 and Ca6) and is not expected to show strong L_2 and L_3 edge splitting because the
301 percentage of octahedral-like sites is relatively low (11.1% for summation of Ca1 and
302 Ca2, 11.1% for Ca3, as shown in Table 1). The Ca $L_{2,3}$ -edge NEXAFS spectrum for
303 C_3A_{cub} is consistent with this line of reasoning, and the complex coordinations of Ca4,
304 Ca5 and Ca6 produce cubic-like crystal field splitting effects with negative $10Dq$.

305

306 The symmetry and size of the unit cell (Table 1) as well as the configurations of Ca
307 atoms (Figure 6) in C_3A_{orth} and C_3A_{cub} are different. In C_3A_{orth} , only Ca3 is in distorted
308 octahedral coordination, with Ca-O bond lengths ranging from 2.31 to 2.409 Å
309 (averaging at 2.355 Å). The other Ca atoms have irregular symmetries but higher
310 coordination numbers (8 for Ca1, Ca2 and Ca4, and 7 for Ca5). Each of the 8-coordinated
311 Ca atoms has four short Ca-O bonds (2.2-2.6 Å) and four long Ca-O bonds (2.6-3.5 Å),
312 with average bond lengths of 2.668 Å for Ca1-O, 2.637 Å for Ca2-O and 2.598 Å for
313 Ca4-O. The Ca5 atom has four short Ca-O bonds (2.4-2.5 Å) and three long Ca-O bonds
314 (2.6-3.1 Å), averaging 2.616 Å.

315

316 The previously mentioned symmetries of Ca atoms in C_3A_{orth} explains the cubic-like Ca
317 $L_{2,3}$ edge NEXAFS spectrum that was measured for this phase (Figure 3). This spectrum
318 differs from that for C_3A_{cub} by a shift in the location of peak 2 to lower energy and a
319 more broadened peak b1, with otherwise minor differences in spectral line shape and
320 peak positions. The energy differences between peaks a2 and a1 and b2 and b1 are
321 slightly smaller in the Ca $L_{2,3}$ edge NEXAFS spectrum for C_3A_{orth} relative to C_3A_{cub} ,
322 indicating a slightly weaker crystal field of Ca in C_3A_{cub} . The doping of Na is not uniform

323 on the unit cell scale, leading to a fractional occupancy of Ca1, which breaks the perfect
324 periodicity over long ranges (Nish and Takeuchi 1975). This may explain the broadening
325 of peak b1 in the C_3A_{orth} spectrum. The sharpening of peak 2 in the spectrum of C_3A_{orth}
326 could then be explained by the higher fraction of octahedral-like coordinated Ca3 atoms
327 in C_3A_{orth} (23.5%) relative to C_3A_{cub} (11.1% for each of the two octahedral-like
328 coordinated sites), whose a1 peak is sharp (de Groot et al. 1990). Therefore, the Ca atoms
329 in C_3A_{orth} are in cubic-like coordination with slightly weaker crystal fields than those in
330 C_3A_{cub} .

331

332 **Absorption saturation**

333 In a transmission X-ray spectroscopy experiment, NEXAFS spectra become ‘saturated’
334 once the sample thickness reaches a limiting value. Increasing sample thickness beyond
335 this limit results in significantly broadened absorption peaks and increases the peak
336 intensity ratio (PIR) of the minor peaks relative to the major peaks. The Ca $L_{2,3}$ -edge
337 NEXAFS spectra collected for ettringite, gypsum and kuzelite samples of different
338 thickness show that the PIRs of the leading and minor peaks typically increase with
339 increasing sample thickness (Figure 7 and Figure 8b). Peaks 2 and b₁₀ in the Ca $L_{2,3}$ -edge
340 NEXAFS spectrum for gypsum, as well as peak 2 for ettringite, become increasingly
341 difficult to resolve as the sample thickness increases. Most of the major peaks and some
342 of the minor peaks in the Ca $L_{2,3}$ -edge NEXAFS spectra for ettringite and gypsum
343 become significantly broadened with increasing sample thickness, although the minor
344 peaks (1, 2, a₁, a₂) in the Ca $L_{2,3}$ -edge NEXAFS spectra for kuzelite do not display peak
345 broadening. This is explained by the perfect or near-perfect crystal structure of the

346 kuzelite crystallites sampled (Figure 3c), such that relatively low amounts of structural-
347 disorder-induced interpeak states are encountered for this phase. Unsurprisingly, peak
348 positions remain unchanged during absorption saturation for all measured phases,
349 meaning that individual phases in composite geochemical systems can be resolved by
350 STXM using this parameter. The features located between 356 and 358 eV are artifacts
351 caused by dynamic focusing of the zone plate.

352

353 Using maximum OD values to estimate sample thickness is a common approach (Hanhan
354 et al. 2009). However, it could be impractical when the background absorption is
355 comparable to the resonance absorption, which frequently occurs in thick sampling
356 regions. Here, we propose another estimation of sample thickness. Sample thickness can
357 be estimated using the Beer-Lambert Law (eqs.(1-2)):

$$358 \quad I = I_0 e^{-\mu t} \quad (1)$$

$$359 \quad OD = \mu t = -\ln(I/I_0) \quad (2)$$

360 where I_0 and I are the incident and transmitted beam intensities, respectively, t is the
361 sample thickness, and μ is the attenuation coefficient (Hubbell and Seltzer 1995).
362 Although μ is a function of the incident beam energy, it can be treated as a constant if the
363 incident beam energy ranges within several tens of eV outside of an absorption edge
364 (Figure 8a). At the absorption edge, μ changes drastically with a small range of variation
365 in beam energy. Beyond the absorption edge, μ once again changes immeasurably with
366 beam energy, as illustrated in Figure 8a. The difference between the pre-edge and post-
367 edge OD, i.e., the optical density difference (ΔOD), is related to t and $\Delta\mu$, i.e., the
368 difference in μ over this same energy range (eq.(3)):

369
$$\Delta OD = \Delta \mu t \tag{3}$$

370 Values of minor to major PIRs in unnormalized Ca $L_{2,3}$ -edge NEXAFS spectra with
371 different ΔOD are shown in Figure 8b. Given the same ΔOD , the PIRs of ettringite,
372 gypsum and kuzelite are similar despite differences in attenuation coefficients and sample
373 densities. For example, using $I(b_1)/I(b_2)$ at $\Delta OD=0.4$, the PIR of these minerals vary
374 within the range 0.75-0.8. These results indicate that the ΔOD parameter may provide a
375 universal measurement of sample attenuation thickness in STXM studies of
376 heterogeneous microscale systems containing these phases.

377

378 The $I(b_1)/I(b_2)$ curve for kuzelite approaches its lower limit asymptotes at $\Delta OD < 0.1$ and
379 upper limit asymptotes at $\Delta OD \geq 0.6$. The same observation applies to all three curves of
380 ettringite, where the lower limit is at $\Delta OD \sim 0.08$ and the upper limit is $\Delta OD \sim 0.43$. The
381 $I(a_1)/I(a_2)$, $I(2)/I(a_2)$ and $I(1)/I(a_2)$ curves of kuzelite display only lower asymptotes at
382 $\Delta OD < 0.1$ because the ΔOD does not become large enough to cause full saturation in the
383 minor peaks a_1 , 1 and 2. For gypsum, a lower asymptote is not clear due to lack of
384 sampling in the low ΔOD region but an upper asymptote is obtained for $\Delta OD > 0.5$. In
385 the medium ΔOD range (approximately 0.1~0.4), the slope of all PIR curves for these
386 phases increase approximately linearly.

387

388

Implications

389 In this paper, Ca $L_{2,3}$ -edge NEXAFS spectra of katoite, ettringite, gypsum, kuzelite,
390 C_3A_{cub} and C_3A_{orth} were reported using scanning transmission X-ray microscopy (STXM).
391 The unique feature of each absorption spectra was described, and the absorption

392 saturation phenomena was quantitatively studied. The current work provides fundamental
393 evidence which can be used to differentiate the aforementioned phases in STXM study of
394 calcium sulfoaluminate aqueous system. Besides providing reference for studying such
395 system in natural system, our work has implication on cement chemistry scientific
396 community by demonstrating novel methods to investigate unsolved topics, for example,
397 the retardation mechanism of calcium sulfate (hydrates) on the rapid hydration of C₃A,
398 which is critical to understanding the early age performance of fresh concrete mixture.
399 Another potential application of the current methodology lies in the hydration dynamics
400 of calcium sulfoaluminate cement, which is a promising alternative of ordinary Portland
401 cement to reduce the heavy carbon footprint of the cement industry (Justnes 2012). In
402 summary, we expect our work to raise general interest from the cement and concrete
403 research community, since STXM can be a powerful chemical and morphological probe
404 to study a rapidly evolving aqueous system given that the reference spectra are well
405 resolved.

406

407

408

Acknowledgments

409 Guoqing Geng's research at the University of California, Berkeley, is supported by the
410 Chinese Scholarship Council (file No. 201206090127). The authors acknowledge the
411 financial support received from Siam Cement, Thailand. The Advanced Light Source is
412 supported by the Director, Office of Science, Office of Basic Energy Sciences, of the U.S.
413 Department of Energy under Contract No. DE-AC02-05CH11231.

414

415

References

- 416 Albright, T.A., Burdett, J.K., and Whangbo, M.H. (2013) Orbital interactions in
417 chemistry. John Wiley & Sons.
- 418 Allmann, R. (1977) Refinement of the hybrid layer structure $[\text{Ca}_2\text{Al}(\text{OH})_6]^-$
419 $\cdot[1/2\text{SO}_4\cdot 3\text{H}_2\text{O}]^+$. Neues Jahrbuch für Mineralogie, Monatshefte, 136-144.
- 420 Barnes, P., and Bensted, J. (2002) Structure and performance of cements. CRC Press.
- 421 Baur, I. and Johnson, C.A. (2003) Sorption of selenite and selenate to cement
422 minerals. Environmental science & technology, 37(15), 3442-3447.
- 423 Bell, D.R., and Rossman, G.R. (1992) Water in Earth's mantle: the role of nominally
424 anhydrous minerals. Science, 255(5050), 1391.
- 425 Black, L., Garbev, K., Stemmermann, P., Hallam, K.R. and Allen, G.C. (2003)
426 Characterisation of crystalline CSH phases by X-ray photoelectron spectroscopy. Cement
427 and concrete research, 33(6), 899-911.
- 428 Burns, R.G. (1993) Mineralogical applications of crystal field theory (Vol. 5). Cambridge
429 University Press.
- 430 Chen, C., Dynes, J.J., Wang, J., Karunakaran, C., and Sparks, D.L. (2014) Soft X-ray
431 spectromicroscopy study of mineral-organic matter associations in pasture soil clay
432 fractions. Environmental science & technology, 48(12), 6678-6686.
- 433 Chrysochoou, M., and Dermatas, D. (2006) Evaluation of ettringite and hydrocalumite
434 formation for heavy metal immobilization: literature review and experimental
435 study. Journal of Hazardous Materials, 136(1), 20-33.

- 436 Collins, B.A., and Ade, H. (2012) Quantitative compositional analysis of organic thin
437 films using transmission NEXAFS spectroscopy in an X-ray microscope. Journal of
438 Electron Spectroscopy and Related Phenomena, 185(5), 119-128.
- 439 Comodi, P., Nazzareni, S., Zanazzi, P.F., and Speziale, S. (2008) High-pressure behavior
440 of gypsum: a single-crystal X-ray study. American Mineralogist, 93(10), 1530-1537.
- 441 Davidovits, J. (1994) Properties of geopolymer cements. In First international conference
442 on alkaline cements and concretes (Vol. 1, pp. 131-149).
- 443 de Groot, F.M.F., Fuggle, J.C., Thole, B.T., and Sawatzky, G.A. (1990) $L_{2,3}$ X-ray-
444 absorption edges of d^0 compounds: K^+ , Ca^{2+} , Sc^{3+} , and Ti^{4+} in Oh (octahedral)
445 symmetry. Physical Review B, 41(2), 928.
- 446 Fleet, M.E., and Liu, X. (2009) Calcium $L_{2,3}$ -edge XANES of carbonates, carbonate
447 apatite, and oldhamite (CaS). American Mineralogist, 94(8-9), 1235-1241.
- 448 Geng, G., Taylor, R., Bae, S., Hernández-Cruz, D., Kilcoyne, D.A., Emwas, A.H., and
449 Monteiro, P.J. (2015) Atomic and nano-scale characterization of a 50-year-old hydrated
450 C_3S paste. Cement and Concrete Research, 77, 36-46.
- 451 Goetz-Neunhoeffler, F. and Neubauer, J. (2006) Refined ettringite ($Ca_6Al_2(SO_4)_3(OH)_{12} \cdot$
452 $26H_2O$) structure for quantitative X-ray diffraction analysis. Powder Diffraction, 21(01),
453 4-11.
- 454 Ha, J., Chae, S., Chou, K.W., Tyliczszak, T., and Monteiro, P.J.M. (2012) Effect of
455 polymers on the nanostructure and on the carbonation of calcium silicate hydrates: a
456 scanning transmission X-ray microscopy study. Journal of materials science, 47(2), 976-
457 989.

- 458 Hanhan, S., Smith, A.M., Obst, M., and Hitchcock, A. P. (2009) Optimization of analysis
459 of soft X-ray spectromicroscopy at the Ca 2p edge. *Journal of Electron Spectroscopy and*
460 *Related Phenomena*, 173(1), 44-49.
- 461 Hartman, M.R. and Berliner, R. (2006) Investigation of the structure of ettringite by time-
462 of-flight neutron powder diffraction techniques. *Cement and Concrete Research*, 36(2),
463 364-370.
- 464 Hashem, F.S. and Amin, M.S. (2014) Kinetic and thermal studies of removal of CrO_4^{2-}
465 ions by ettringite. *Journal of Thermal Analysis and Calorimetry*, 116(2), 835-844.
- 466 Hillier, S., Lumsdon, D.G., Brydson, R., and Paterson, E. (2007) Katoite: A host phase
467 for Cr (VI) in chromite ore processing residue (COPR) and other high pH
468 wastes. *Environmental science & technology*, 41(6), 1921-1927.
- 469 Hitchcock, A.P., Hitchcock, P., Jacobsen, C., Zimba, C., Loo, B., Rotenberg, E.,
470 Denlinger, J., and Kneedler, R. (2012) *aXis 2000 — Analysis of X-ray Images and*
471 *Spectra*. McMaster University, Hamilton.
- 472 Hubbell, J.H., and Seltzer, S.M. (1995) Tables of X-ray mass attenuation coefficients and
473 mass energy-absorption coefficients 1 keV to 20 MeV for elements $z = 1$ to 92 and 48
474 additional substances of dosimetric interest (No. PB--95-220539/XAB; NISTIR--5632).
475 National Inst. of Standards and Technology-PL, Gaithersburg, MD (United States).
476 Ionizing Radiation Division.
- 477 Jackson, M.D., Chae, S.R., Mulcahy, S.R., Meral, C., Taylor, R., Li, P., Emwas, A.H.,
478 Moon, J., Yoon, S., Vola, G., Wenk, H.R., and Monteiro, P.J.M. (2013) Unlocking the

- 479 secrets of Al-tobermorite in Roman seawater concrete. *American Mineralogist*, 98(10),
480 1669-1687.
- 481 Justnes, H. (2012) Alternative low-CO₂ “green” clinkering process. *Reviews in*
482 *Mineralogy and Geochemistry*, 74(1), 83-89.
- 483 Kilcoyne, A.L.D., Tyliczszak, T., Steele, W.F., Fakra, S., Hitchcock, P., Franck, K.,
484 Anderson, E., Harteneck, B., Rightor, E.G., Mitchell, G.E. and Hitchcock, A.P. (2003)
485 Interferometer-controlled scanning transmission X-ray microscopes at the Advanced
486 Light Source. *Journal of Synchrotron Radiation*, 10(2), 125-136.
- 487 Lager, G.A., Armbruster, T., and Faber, J. (1987) Neutron and X-ray diffraction study of
488 katoite Ca₃Al₂(O₄H₄)₃. *American Mineralogist*, 72(7-8), 756-765.
- 489 McNeill, C. R., Watts, B., Swaraj, S., Ade, H., Thomsen, L., Belcher, W., and Dastoor, P.
490 C. (2008) Evolution of the nanomorphology of photovoltaic polyfluorene blends: sub-100
491 nm resolution with X-ray spectromicroscopy. *Nanotechnology*, 19(42), 424015.
- 492 Mehta, P.K., and Monteiro, P.J.M (2014) *Concrete: microstructure, properties, and*
493 *materials*. 4th edition. New York: McGraw-Hill.
- 494 Miedema, P.S., Ikeno, H., and de Groot, F.D. (2011) First principles multiplet
495 calculations of the calcium *L*_{2,3} X-ray absorption spectra of CaO and CaF₂. *Journal of*
496 *Physics: Condensed Matter*, 23(14), 145501.
- 497 Mondal, P., and Jeffery, J.W. (1975) The crystal structure of tricalcium aluminate,
498 Ca₃Al₂O₆. *Acta Crystallographica Section B: Structural Crystallography and Crystal*
499 *Chemistry*, 31(3), 689-697.

- 500 Moore, A.E., and Taylor, H.F.W. (1970) Crystal structure of ettringite. Acta
501 Crystallographica Section B: Structural Crystallography and Crystal Chemistry, 26(4),
502 386-393.
- 503 Naftel, S.J., Sham, T.K., Yiu, Y.M., and Yates, B.W. (2001) Calcium L-edge XANES
504 study of some calcium compounds. Journal of Synchrotron Radiation, 8(2), 255-257.
- 505 Nelson, R.E. (1982) Carbonate and gypsum. Methods of Soil Analysis. Part 2. Chemical
506 and Microbiological Properties, 181-197.
- 507 Nishi, F., and Takeuchi, Y. (1975) The $A_{16}O_{18}$ rings of tetrahedra in the structure of
508 $Ca_{8.5}NaAl_6O_{18}$. Acta Crystallographica Section B: Structural Crystallography and Crystal
509 Chemistry, 31(4), 1169-1173.
- 510 Obst, M., Dynes, J.J., Lawrence, J.R., Swerhone, G.D.W., Benzerara, K., Karunakaran,
511 C., Kaznatcheev K., Tyliszczak T., and Hitchcock, A.P. (2009) Precipitation of
512 amorphous $CaCO_3$ (aragonite-like) by cyanobacteria: a STXM study of the influence of
513 EPS on the nucleation process. Geochimica et Cosmochimica Acta, 73(14), 4180-4198.
- 514 Patel, M., and Aswath, P.B. (2012) Morphology, structure and chemistry of extracted
515 diesel soot: part II: X-ray absorption near edge structure (XANES) spectroscopy and high
516 resolution transmission electron microscopy. Tribology International, 52, 17-28.
- 517 Puppala, A.J., Intharasombat, N., and Vempati, R.K. (2005) Experimental studies on
518 ettringite-induced heaving in soils. Journal of Geotechnical and Geoenvironmental
519 Engineering, 131, 325-337.

- 520 Sandford, S.A., Aléon, J., Alexander, C.M.D., Araki, T., Bajt, S., Baratta, G.A., Borg, J.,
521 Bradley, J.P., Brownlee, D.E., Brucato, J.R. and Burchell, M.J. (2006) Organics captured
522 from comet 81P/Wild 2 by the Stardust spacecraft. *Science*, 314(5806), 1720-1724.
- 523 Sasaki, T., Atsushi I., Masayuki W., Teruhisa H., and Akihiro Y. (2014) Preparation and
524 performance of arsenate (V) adsorbents derived from concrete wastes. *Waste*
525 *Management*, 34(10), 1829-1835.
- 526 Skibsted, J., Henderson, E., and Jakobsen, H.J. (1993) Characterization of calcium
527 aluminate phases in cements by aluminum-27 MAS NMR spectroscopy. *Inorganic*
528 *chemistry*, 32(6), 1013-1027.
- 529 Solomon, D., Lehmann, J., Harden, J., Wang, J., Kinyangi, J., Heymann, K., Karunakaran,
530 C., Lu, Y., Wirick, S. and Jacobsen, C. (2012) Micro- and nano-environments of carbon
531 sequestration: Multi-element STXM-NEXAFS spectromicroscopy assessment of
532 microbial carbon and mineral associations. *Chemical geology*, 329, 53-73.
- 533 Stöhr, J. (2013) NEXAFS spectroscopy (Vol. 25). Springer Science & Business Media.
- 534 Taylor, H.F.W. (1997) 2nd edition. *Cement chemistry*. Thomas Telford.
- 535 van Aardt, J.H., and Visser, S. (1977) Formation of katoites: calcium hydroxide attack on
536 clays and feldspars. *Cement and Concrete Research*, 7(1), 39-44.
- 537 Wan, J., Tyliczszak, T., and Tokunaga, T.K. (2007) Organic carbon distribution,
538 speciation, and elemental correlations within soil microaggregates: applications of STXM
539 and NEXAFS spectroscopy. *Geochimica et Cosmochimica Acta*, 71(22), 5439-5449.
- 540 Warwick, T., Ade, H., Kilcoyne, D., Kritscher, M., Tyliczszak, T., Fakra, S., Hitchcock,
541 A., Hitchcock, P. and Padmore, H. (2002) A new bend-magnet beamline for scanning

542 transmission X-ray microscopy at the Advanced Light Source. *Journal of Synchrotron*
543 *Radiation*, 9(4), 254-257.

544 Zhou, Q., Milestone, N.B., and Hayes, M. (2006) An alternative to Portland cement for
545 waste encapsulation — the calcium sulfoaluminate cement system. *Journal of hazardous*
546 *materials*, 136(1), 120-129.

547

548

Figure captions

549 **Figure 1.** Representation of the crystal field splitting of 3*d* orbitals in cubic and
550 octahedral coordination states in Ca²⁺. Here, the central atoms (solid blue circles) are Ca
551 and the coordinated atoms (hollow circles) are oxygen. Descriptions of the various
552 parameters depicted are described in the text. Adapted from Burns (1993).

553 **Figure 2.** Schematic representation of a sample in the instrument chamber for Ca *L*_{2,3}-
554 edge NEXAFS and STXM analysis (not to scale).

555 **Figure 3.** (a) Ca *L*_{2,3}-edge NEXAFS spectra of ettringite, kuzelite, katoite, gypsum,
556 C₃A_{cub} and C₃A_{orth}, collected from the regions in (b)-(g). The absorption signals of the
557 dashed circle or straight lines in each image were averaged to yield the spectra. Insets are
558 spectra of CaF₂ (de Groot et al. 1990) and Ca(OH)₂ (Geng et al. 2015) as examples of
559 cubic and octahedral coordination, respectively.

560 **Figure 4.** Coordination environments of Ca in (a) katoite (Lager et al. 1987), (b)
561 ettringite (Moore and Taylor 1970), (c) kuzelite (Allmann 1977) and (d) gypsum (Comdi
562 et al. 2008)0, with rotation axes marked by dashed lines. The insets show color blocks
563 that illustrate the orientations of coplanar oxygen atoms viewed down the rotation axes.
564 Filled triangles represent three-fold axes. Arrow ends and filled ellipses represent two-
565 fold axes. Bond lengths are in Å.

566 **Figure 5.** Coordination environments of the six Ca sites in the C₃A_{cub} unit cell (Mondal
567 and Jeffery 1975): (a) Ca1; (b) Ca2; (c) Ca3; (d) Ca4; (e) Ca5; and (f) Ca6. Angles are
568 marked with red labels.

569 **Figure 6.** Coordination environments of the five Ca sites in the C_3A_{orth} unit cell (Nishi
 570 and Takeuchi 1975): (a) Ca1; (b) Ca2; (c) Ca3; (d) Ca4 and (e) Ca5.

571 **Figure 7.** Ca $L_{2,3}$ -edge NEXAFS spectra of (a) ettringite, (b) gypsum and (c) kuzelite in
 572 samples of different thickness. The features located between 356 and 358 eV are
 573 measurement artifacts.

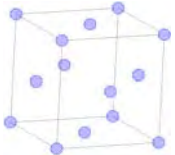
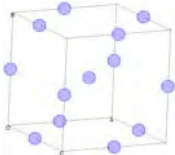
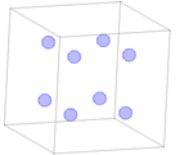
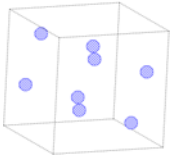
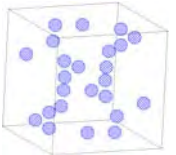
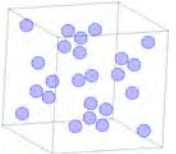

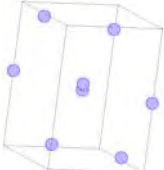
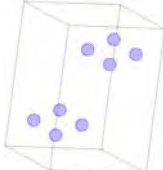
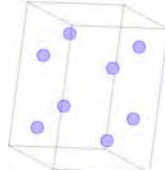
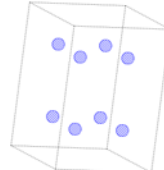
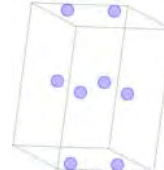
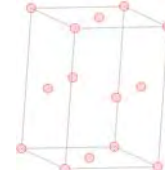

574 **Figure 8.** (a) Sample thickness parameters indicated for a Ca $L_{2,3}$ -edge NEXAFS
 575 spectrum of calcium monosulfoaluminate hydrate. (b) PIRs for ettringite, gypsum and
 576 calcium monosulfoaluminate hydrate as functions of ΔOD .

577

578

Tables

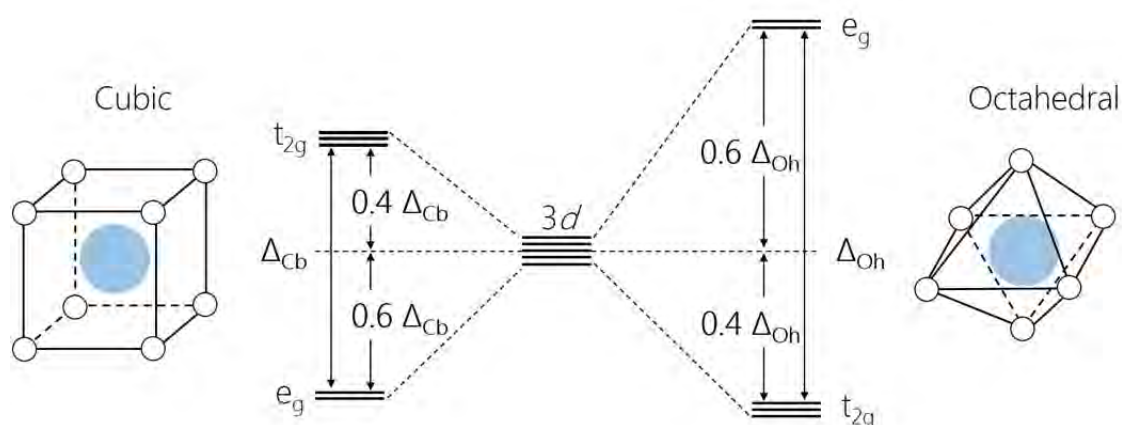
579 **Table 1.** Numbers and locations of Ca and Na atoms in the C_3A_{cub} (Mondal and Jeffery
 580 1975) and C_3A_{orth} unit cells (Nishi and Takeuchi 1975).

		Ca1	Ca2	Ca3	Ca4	Ca5	Ca6
Number of atoms		4	4	8	8	24	24
C_3A_{cub}	View from (-0.4, 0.7, 1.5)						
							
		Ca1	Ca2	Ca3	Ca4	Ca5	Na
Number of atoms		2 (occupancy 0.25)	8	8	8	8	4
C_3A_{orth}	View from (-1.5, 1, -0.24)						
							

581

582

Figures



583

584

Figure 1. Representation of the crystal field splitting of 3d orbitals of Ca²⁺ in cubic and

585

octahedral coordinations. Here, the central atoms (solid blue circles) are Ca and the

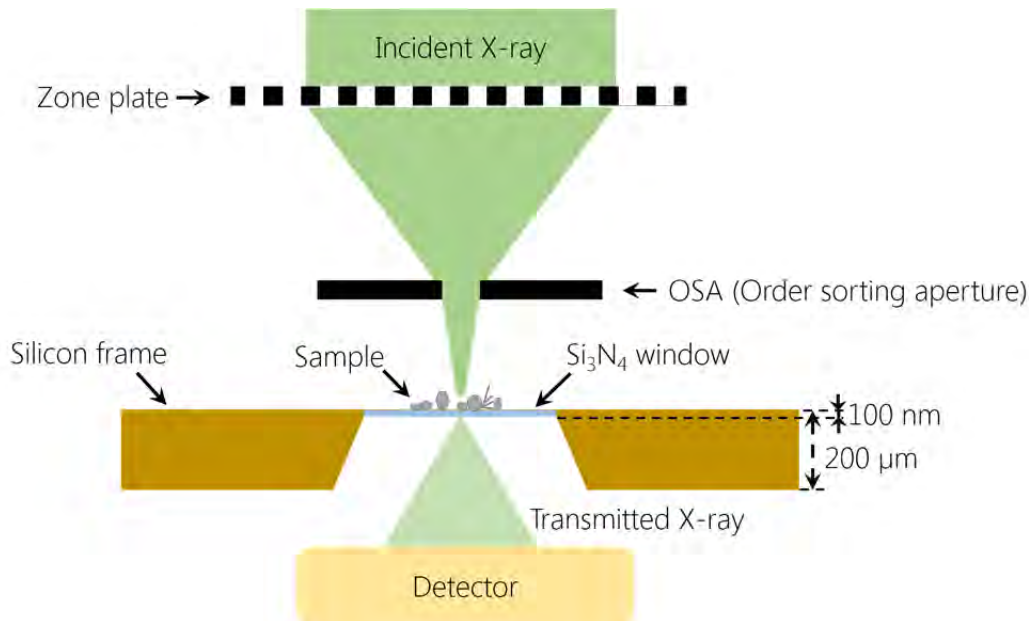
586

coordinated atoms (hollow circles) are oxygen. Descriptions of the various parameters

587

depicted are described in the text. Adapted from Burns (1993).

588



589

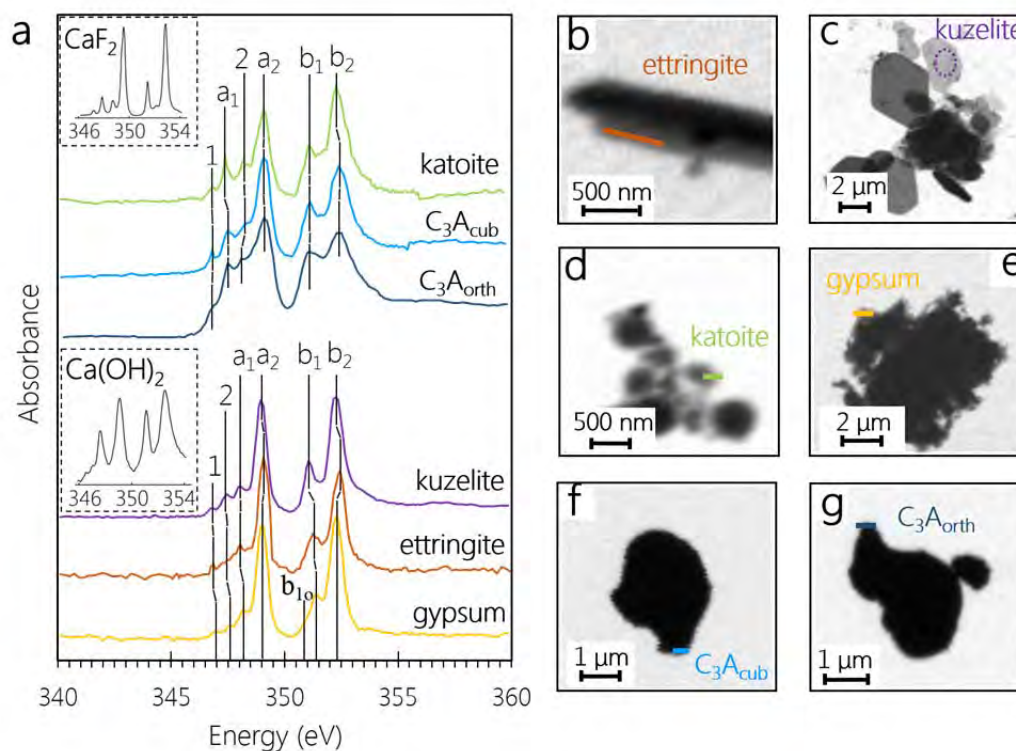
590

Figure 2. Schematic representation of a sample in the instrument chamber for Ca $L_{2,3}$ -

591

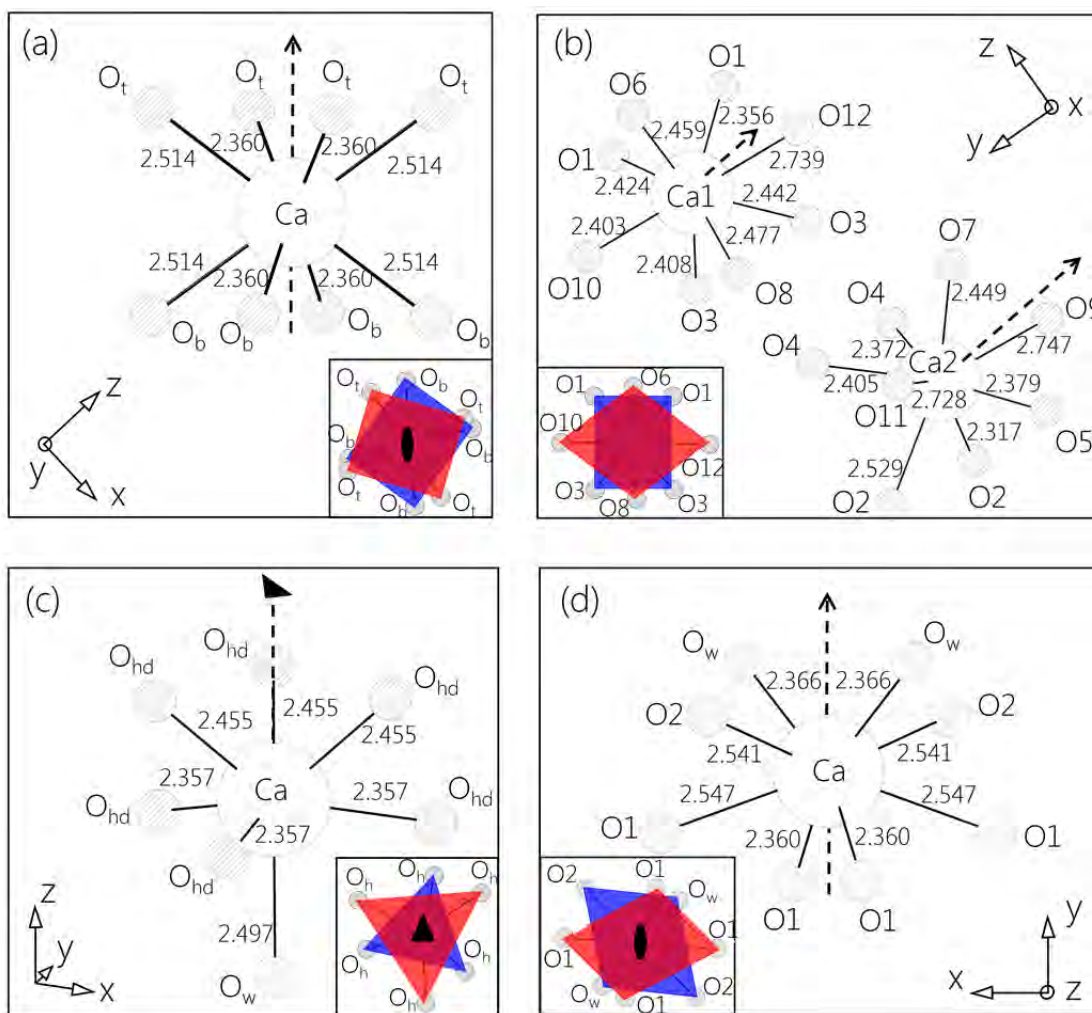
edge NEXAFS and STXM analysis (not to scale).

592



593
594
595
596
597
598
599

Figure 3. (a) Ca $L_{2,3}$ -edge NEXAFS spectra of ettringite, kuzelite, katoite, gypsum, C_3A_{cub} and C_3A_{orth} , collected from the regions in (b)-(g). The absorption signals of the dashed circle or straight lines in each image were averaged to yield the spectra. Inset are spectra of CaF_2 (de Groot et al. 1990) and $Ca(OH)_2$ (Geng et al. 2015) as examples of cubic and octahedral coordination, respectively.



600
601

Figure 4. Coordination environments of Ca in (a) katoite (Lager et al. 1987), (b)

602

ettringite (Moore and Taylor 1970), (c) kuzelite (Allmann 1977) and (d) gypsum (Comdi

603

et al. 2008), with rotation axes marked by dashed lines. The insets show color blocks that

604

illustrate the orientations of coplanar oxygen atoms viewed down the dash arrows. Filled

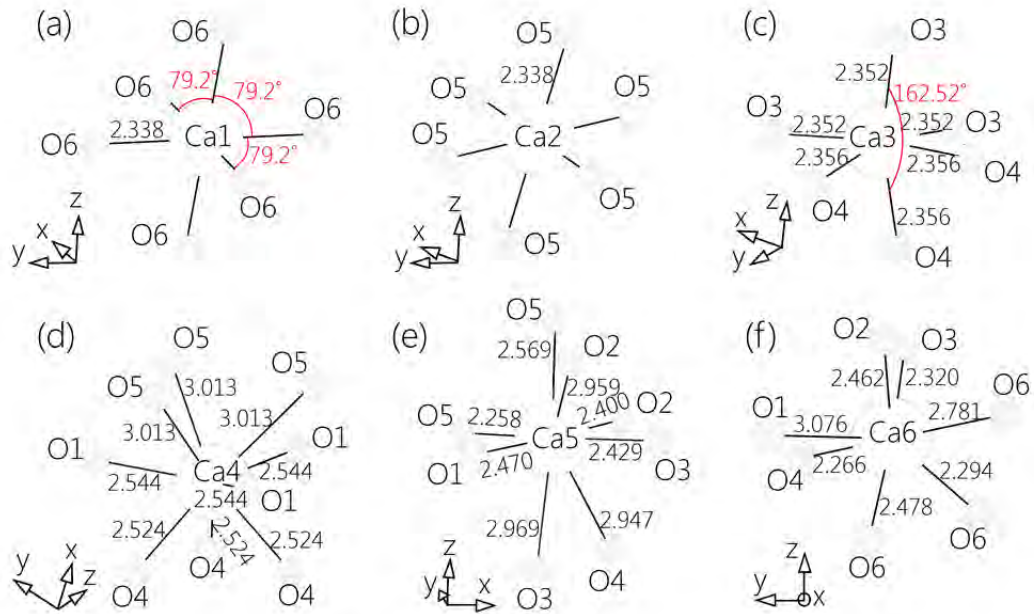
605

ellipses represent two-fold axes. Filled triangles represent three-fold axes. Bond lengths

606

are in Å.

607



608

609

Figure 5. Coordination environments of the six Ca sites in the C_3A_{cub} unit cell

610

(Mondal and Jeffery 1975): (a) Ca1; (b) Ca2; (c) Ca3; (d) Ca4; (e) Ca5; and (f) Ca6.

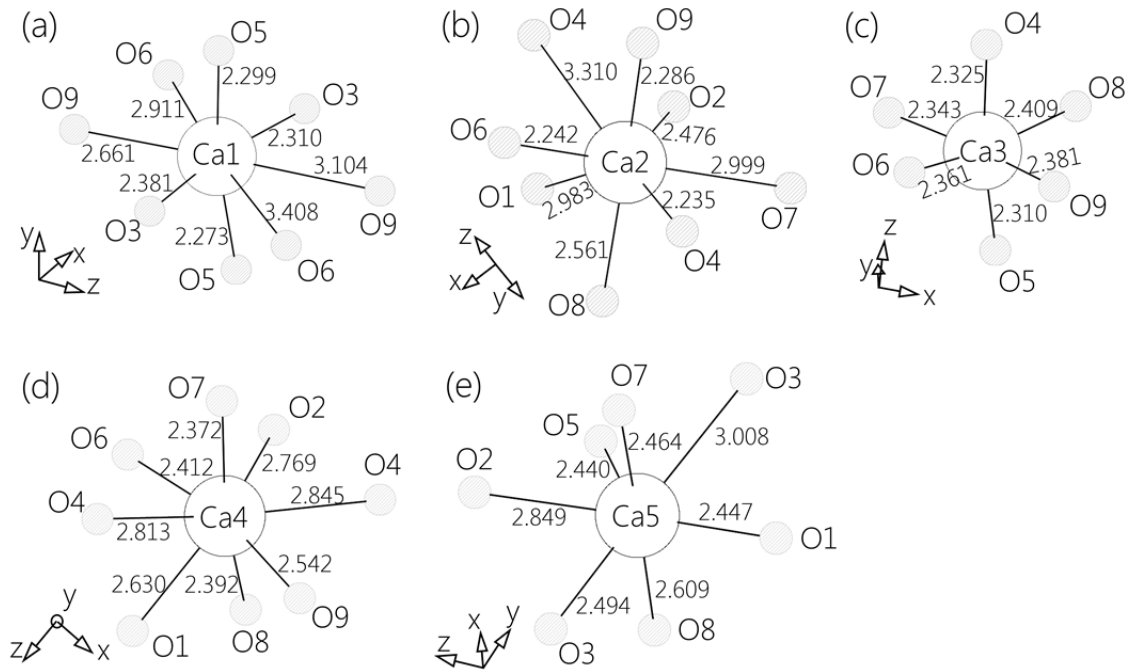
611

Angles are marked with red labels.

612

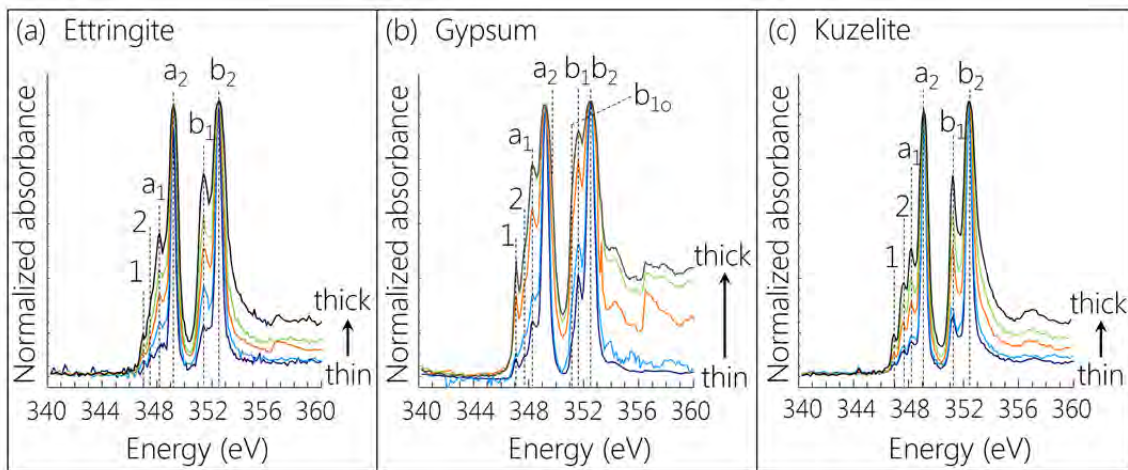
613

614



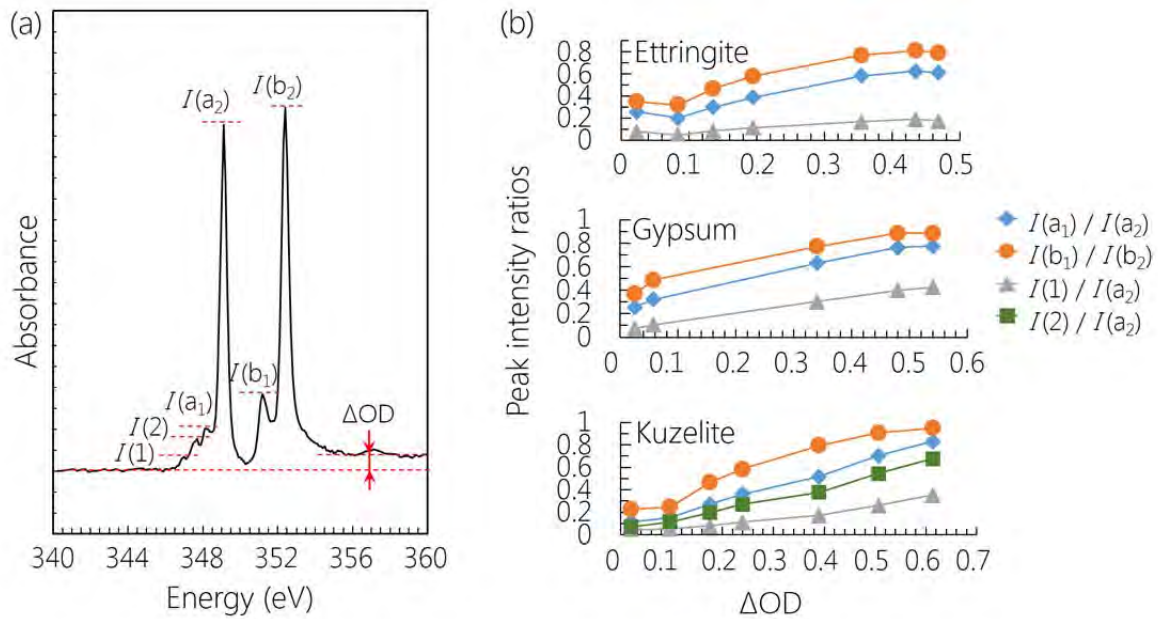
615
 616 **Figure 6.** Coordination environments of the five Ca sites in the C_3A_{orth} unit cell (Nishi
 617 and Takeuchi 1975): (a) Ca1; (b) Ca2; (c) Ca3; (d) Ca4 and (e) Ca5.

618
 619



620
 621 **Figure 7.** Ca $L_{2,3}$ -edge NEXAFS spectra of (a) ettringite, (b) gypsum and (c) kuzelite in
 622 samples of different thickness. The features located between 356 and 358 eV are
 623 measurement artifacts.

624



625

626

Figure 8. (a) Sample thickness parameters indicated for a Ca $L_{2,3}$ -edge NEXAFS

627

spectrum of calcium monosulfoaluminate hydrate. (b) PIRs for ettringite, gypsum and

628

calcium monosulfoaluminate hydrate as functions of ΔOD .

629